Structure, Processing, Morphology, and Property Relationships of Biaxially Drawn Ziegler–Natta/Metallocene Isotactic Polypropylene Film

ROGER A. PHILLIPS, TINH NGUYEN

Basell USA Inc., Research and Development Center, 912 Appleton Road, Elkton, Maryland 21921

ABSTRACT: The structure, processing, morphology, and property relationships of biaxially drawn isotactic polypropylene (BOPP) film of mixed metallocene isotactic PP (m-iPP) and Ziegler–Natta iPP (ZN-iPP) homopolymer compositions are developed. The DSC and film drawing behavior show cocrystallization of the ZN-iPP and m-iPP components. The structure, processing, morphology, and property relations of ZN-iPP/m-iPP blends are compared with ZN-iPP of varying isotacticities. The ZN-iPP/m-iPP blends exhibit reduced biaxial yield stress [$\sigma_y(T)$]. A fractional crystallinity model collapses the $\sigma_y(T)$ data into a common normalized form over a range of draw temperatures, ZN-iPP tacticities, and blend compositions. The simplified model is extended to define the interrelationships of yield activation and strain hardening behavior into regimes differentiated by characteristic draw stress (crystallinity) levels. Structure–property models are developed to explain the effect of draw temperature and resin–blend microstructure on the draw behavior, film stiffness, barrier, elongation, and synergies of the BOPP film processing–property balance. © 2001 John Wiley & Sons, Inc. J Appl Polym Sci 80: 2400–2415, 2001

Key words: polypropylene; biaxial orientation; metallocene; Ziegler–Natta

INTRODUCTION

The formation of biaxially oriented isotactic polypropylene (BOPP) film can be viewed as a specialized case of the more general physical problem of semicrystalline polymer drawing.[1–8] During BOPP film formation, a cast sheet of isotactic polypropylene (iPP) is drawn below the melting point in two directions. This drawing process creates a film of useful dimensions while imparting desired properties such as barrier and stiffness. These properties are related to the imposed orientation during drawing. The elevated temperature stress–strain curve during tensile extension is a useful record of the morphological transformation that occurs during drawing. This stress–strain curve is illustrated schematically in Figure 1. The schematic is divided into four regions (I–IV) according to uniaxial deformation models of semicrystalline polymers.[2–4,8]

Region I is characterized by reversible deformation at low strain and the onset of irreversible deformation at slightly higher strains. The irreversible deformation is associated with both amorphous chain stretching and lamellar reorientation.[8] In unoriented starting material, the modulus in region I is strongly correlated to the degree of crystallinity and deformation temperature.[9–21] Other contributing morphological factors have been cited,[13,15,18–20,22] but crystallin-
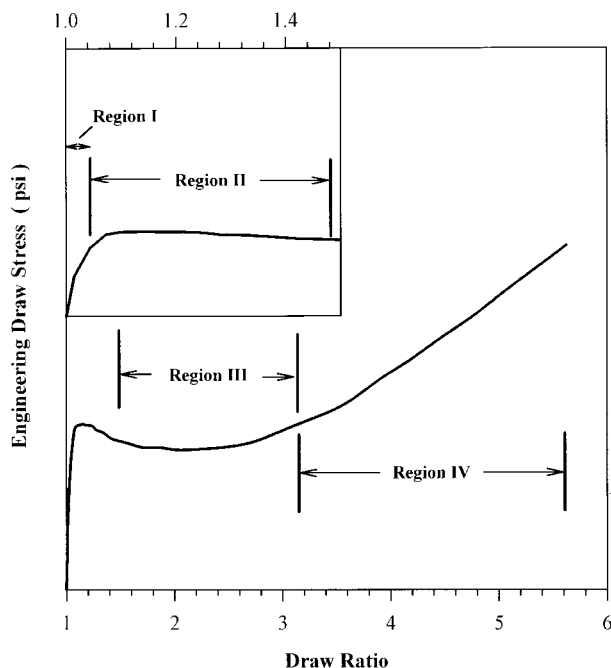
Figure 1 The morphological regions of the draw stress curve. See text for discussion.

ity is a dominant variable. Region II is the yield region, and it represents the onset of plastic deformation. Partial disruption of crystallites is initiated in this region. Region III is the draw stress region. This region is associated with the gradual transformation of the lamellar morphology to an oriented fibrillar morphology.[2-4,8] Deformation in regions III and IV may be extremely restricted if stretching conditions or resin structure are not well suited to drawing. Near the end of region III the fibrillar morphology is well established, and the "strain-hardened" region IV is associated with fiberlike deformation of oriented fibrillar morphology. Region IV deformation is influenced by the tie molecule concentration induced by the drawing process with increasing draw ratio.[3,4] The morphological origins of these regions, while understood in general terms for uniaxial deformation, is poorly understood for biaxial orientation, despite the long-standing commercial utilization of the BOPP method.

The molecular origins of yielding (region II) in semicrystalline polymers also remains somewhat of an open issue.[5,7,8,15,23-25] Two very general viewpoints have been proposed. The first is that of melting and recrystallization (RM) during deformation,[23,25] and the second is the proposal of crystallographic slip (CS) mechanisms.[5,15,18,24] Both proposals focus on the semicrystalline nature of

the material, despite the fact that yielding is also observed in glassy amorphous polymers.[5] All models require local disruption of intermolecular "contacts" during yield in the form of cooperative intermolecular motion in amorphous polymers,[26] a local melting and oriented recrystallization in the RM model,[23,25] or CS in the CS model.[5,8,15] Irrespective of the model, the yield in semicrystalline polymers is associated with the onset of lamellar–crystallite disruption as a precursor to the development of oriented morphologies. The disruption is viewed as a thermally activated process in phenomenological models,[27-29] which accounts for the long-established observation that the yield stress at fixed crystallinity decreases with increasing temperature and decreasing strain rate.[27,29] The yield–morphology relationships are complicated. Among other factors, the crystallinity[7,8,15,16,19,21,22] and crystallite size[5,15,24] are viewed as most important. Crystallinity is clearly a dominant variable in semicrystalline polymers.[19,22]

In Ziegler–Natta iPP (ZN-iPP), tacticity is a critical factor influencing the crystallinity (and subsequent yield behavior).[20,30-32] Details of the interchain tacticity distribution[32] influence not only the crystallinity at room temperature but also the partial melting behavior at elevated temperature. Generally a shift of the interchain tacticity distribution to lower melting fractions will reduce the crystallinity at the draw temperature, reduce the corresponding yield stress, and promote drawing at lower temperature. However, the fractions that are molten at the draw temperature can also recrystallize on cooling. Because this crystallization process may not necessarily retain the high orientation of the drawn material, which is solidlike at the stretch temperature, the tacticity distribution can indirectly influence not only the drawability and crystallinity but also the frozen-in orientation of the final article. In ZN-iPP a decrease in resin tacticity (promoting drawability) is invariably accompanied by decreasing crystallinity[30-32] and subsequently adverse properties (such as stiffness and barrier) in the final film. This implies a processability–property trade-off in the design of BOPP resins from ZN-iPP.

In contrast to ZN-iPP, iPP from metallocene catalysts (m-iPP) can show appreciable levels of regiomisinsertion errors (vs. tacticity errors) in chains of high stereospecificity.[33-46] The melting point of m-iPP is tunable, not only by tacticity (as in ZN-iPP), but also by the level of regiomisinser-

Table I   Material Set

Sample	MFR (g/10 min)	M_w	M_w/M_n	XSRT (%)	mm (%) ^{13}C-NMR	SUE ^{13}C-NMR	ΔH (J/gm)	T_m (°C)
LT-iPP	3.8	350,000	5.8	5.67	91.3	17.1	90.3	162.5
MT-iPP	3.5	350,000	4.7	4.99	92.1	11.7	95.4	163.3
HT-iPP	4.4	330,000	5.1	1.57	97.8	2.5	106.6	166.7
HMT-iPP/m-iPP (60/40)	4.2	340,000	3.9	—	—	—	95.4	159.3
HHT-iPP/m-iPP (60/40)	4.7	360,000	4.6	—	—	—	102.0	162.7
HMT-iPP matrix	0.83	—	—	4.53	90.8	15.1	94.7	162.6
HHT-iPP matrix	0.88	—	—	2.42	96.3	4.0	105.3	167.1
m-iPP	27.7	190,000	2.2	0.47	95.2	12.6[a]	93.8	148.3

SUE, ^{13}C-NMR single unit stereoerror content per 1000 monomer units in the isotactic fraction based on a two-site enantiomorphic model.[50]

[a] The resin contains 0.35 mol % {2,1}-erythro regiomisinsertions.

tions.[33–35,40,47] Recent work demonstrated that m-iPP can expand the crystallinity–melting point property map of ZN-iPP to lower melting structures.[33] This implies a potential shift in the processing–property balance in BOPP applications relative to ZN-iPP. However, m-iPP also exhibits a narrowed interchain tacticity and molecular weight distribution relative to ZN-iPP.[33–35,47,48] When used as a homopolymer, the narrow interchain tacticity distribution is expected to be a significant limitation of m-iPP in BOPP applications due to a narrowing of the temperature window for stretching.[49] This led to mixed catalyst strategies when using all metallocene BOPP formulations.[49] Using m-iPP in conjunction with ZN-iPP offers a similar approach.

This study examines ZN-iPP/m-iPP homopolymer blends in BOPP film applications. Structure, processing, morphology, and property models are developed to explain the effect of draw temperature, ZN-iPP tacticity, and ZN-iPP/m-iPP blend composition on the draw behavior, morphology, film stiffness, barrier, elongation, and synergies of the BOPP film processing–property balance.

EXPERIMENTAL

Table I summarizes the material set and the melt flow rate (MFR); GPC weight-average molecular weight and polydispersity (M_w, M_w/M_n); the percent xylene solubles, which is a measure of atactic content (%XSRT); the ^{13}C-NMR isotactic triad

percentage (mm%); a ^{13}C-NMR measure of single unit stereoerrors (SUE); and the heat of fusion (ΔH) and melting point (T_m) derived from reheat DSC scans. The SUE parameter is intended to represent the single unit stereoerrors per 1000 monomer units in the isotactic fraction based on a two-site enantiomorphic model.[50] Three ZN-iPP homopolymers were studied and given the designations LT-iPP, MT-iPP, and HT-iPP corresponding to low, medium, and high tacticity resins. These broad classifications were based on the general qualitative combined ranking of %XSRT, ^{13}C-NMR measures of tacticity, ΔH, and melting point data. Melting point and crystallinity generally increase with increasing tacticity as reviewed in detail elsewhere.[30–33] Also included in Table I is the regiomisinsertion content for the m-iPP sample. The ZN-iPP/m-iPP blends utilize a high molecular weight MT and HT ZN-iPP matrix. The properties of the matrix materials are given in Table I. The fractional melt flow ZN-iPP matrix (~0.8 MFR) was blended with the high melt flow m-iPP (~28 MFR) to form 60/40 wt % ZN-iPP/m-iPP blends. The blend based on the high molecular weight MT matrix was given the designation HMT-iPP/m-iPP. The blend based on the high molecular weight HT matrix was given the designation HHT-iPP/m-iPP. The final MFR and weight-average molecular weight of the blends closely matched the ZN-iPP LT, MT, and HT resins. The blends and ZN-iPP resins were all pelletized on a Leistritz twin screw extruder at 250

rpm with a 234°C melt temperature and a 25 lb/h feed rate with common stabilization packages.

The pelletized materials were cast into a 0.635 mm thick sheet on a Killion extruder (3.81-cm screw diameter, length/diameter ratio = 30) fitted to a 25.4-cm flat die for vertical extrusion at 50 rpm and 250°C. The sheets were quenched on a water cooled chill roll (35–40°C) set at a draw speed of 2.5 m/min. Wide-angle X-ray scattering measurements from the as-cast sheet showed predominantly α-form crystallinity[32] for all samples, and there were only trace levels of β-form crystallinity[32] and no γ-form crystallinity.[32] Sections of cast sheet were subsequently biaxially oriented into BOPP film using a TM long stretcher. This equipment allows for the four-side clamping of a 5.08×5.08 cm specimen with simultaneous stretching under controlled temperature. A transducer for high temperature operation is mounted on the clamp system and interfaced with a personal computer for *in situ* engineering stress–strain measurements. Simultaneous biaxially oriented film was drawn at temperatures of 135–160°C in 5°C increments. The draw ratio from the initial 5.08-cm square gauge length was 6×6. The strain rate was 9000%/min following a 45-s preheating at the draw temperature. The final film thickness was generally on the order of 0.0254 mm. The *in situ* stress–strain curves were derived from an engineering stress calculation based on the initial sheet cross section.

All the BOPP films were aged at 23°C and 50% relative humidity for 1 week prior to physical testing. Tensile characterization of the films was performed on an Instron 4400R according to ASTM D 882 with a strain rate of 50.8 cm/min for measurement of the ultimate properties and 2.54 cm/min for measurement of the modulus. The modulus (1% secant) and ultimate elongation were calculated. Oxygen transmission rate measurements were performed according to ASTM D 3985-81 at 23.3°C. Samples of the as-cast sheet and drawn film were characterized with differential scanning calorimetry (DSC) on a Perkin–Elmer DSC 7. The DSC 7 was calibrated with indium and mercury at 20°C/min and purged with nitrogen. Heat–cool–reheat ramps were applied over a temperature range from −55 to 235°C using the as-cast sheet. The drawn film was characterized as received. The heat of fusion and crystallization were determined by a method that establishes the solid–melt baseline by an iterative technique to allow the transition from solid to melt baselines in proportion to the loss in crystallinity. The baseline subtracted excess heat capacity was used to calculate the fractional melting–crystallinity arrays from the reheat scans. The $f(T)$ is the percentage of the total DSC endotherm area that is melted at a temperature T and is termed the fractional melting parameter. The ΔH_{reheat} is the total heat of fusion (proportional to crystallinity) of the reheat DSC scan. The term $(1 - f)\Delta H_{\text{reheat}}$ is an *empirical* parameter that is intended to qualitatively represent the crystallinity at the draw temperature. Limitations of the parameter are discussed later. An equilibrium heat of fusion (ΔH°) for 100% crystalline iPP[32] of 165 J/g was assumed to calculate an empirical temperature dependent crystallinity index $[(1 - f)\Delta H_{\text{reheat}}/\Delta H^{\circ}]$. The choice of the ΔH° parameter, which was reported over a considerable range,[32] did not influence the conclusions here. Density measurements of the as-drawn film were performed using a 2-propanol and water density gradient column. As a point of reference, the density of iPP in the α form varies between the limit for 100% amorphous ($\rho_a = 0.850-0.855$ g/cm^3) and 100% crystalline ($\rho_c = 0.936-0.946$ g/cm^3).[32]

RESULTS

Draw Behavior

Figure 2 shows the engineering biaxial yield stress (σ_y) data for each sample in Table I spanning a range of draw temperatures. The ZN-iPP resins and ZN-iPP/m-iPP blends are shown. The behavior shown in Figure 2 is typical of iPP drawn near the melting point. The σ_y decreases sharply with increasing draw temperature over a relatively narrow temperature range. Figure 2 also shows the sensitivity of the elevated temperature draw behavior to the iPP tacticity microstructure. At fixed draw temperature the σ_y decreases in the ZN-iPP resins with decreasing tacticity (HT-iPP > MT-iPP > LT-iPP). Figure 2 also shows that the ZN-iPP/m-iPP blends exhibit lower σ_y relative to the ZN-iPP resin with a melting point comparable to the ZN-iPP matrix component in the blend. This is perhaps seen most clearly in the comparison of HT-iPP with the HHT-iPP/m-iPP blend. The HT-iPP resin and HHT-iPP component in the blend have comparable melting points (Table I), but the blend exhibits much lower σ_y. These results confirm that the addition of a low melting m-iPP to a high melting ZN-iPP has considerable influence on the variable temperature draw behavior.
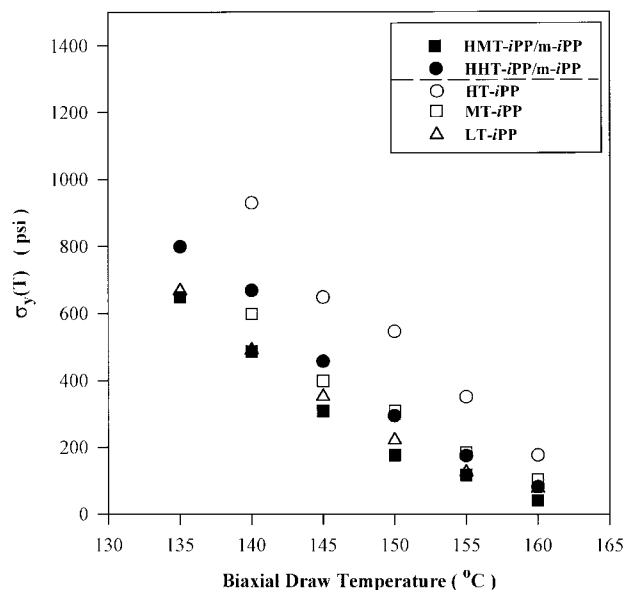
Figure 2 The biaxial engineering yield stress, $\sigma_y(T)$, versus the draw temperature for ZN-iPP (open symbols) and ZN-iPP/m-iPP blends (filled symbols).

Figure 3 quantitatively defines other features of the biaxial stress–strain curve at elevated temperature. The σ_{draw} is the draw stress, which is analogous with introductory discussions of region III deformation behavior. In this context, the σ_{draw} is taken as a qualitative measure of the stress required for the lamellar to fibrillar transformation.[2–4,8] The $\sigma_{y,act}$ is defined as the difference between σ_y and σ_{draw} ($\sigma_{y,act} = \sigma_y - \sigma_{draw}$). We termed this quantity the activation stress, because the stress required to initiate crystallite disruption (σ_y) will in general exceed the stress for subsequent drawing (σ_{draw}). This description is consistent with the viewpoint of polymer yielding as an activated process. The σ_{max} is defined as the stress at the final fabrication draw ratio (DR-$_{fin}$ = 6 × 6). The σ_{hard} is defined by the difference between σ_{max} and σ_{draw} ($\sigma_{hard} = \sigma_{max} - \sigma_{draw}$) and quantifies the region IV strain hardening. Figure 4 shows the relationship of σ_{max} or σ_{draw} with the σ_y for all of the samples and draw temperatures investigated. There appears to be a common relationship in both cases, irrespective of the draw temperature or whether the sample is ZN-iPP or a ZN-iPP/m-iPP blend.

Morphology

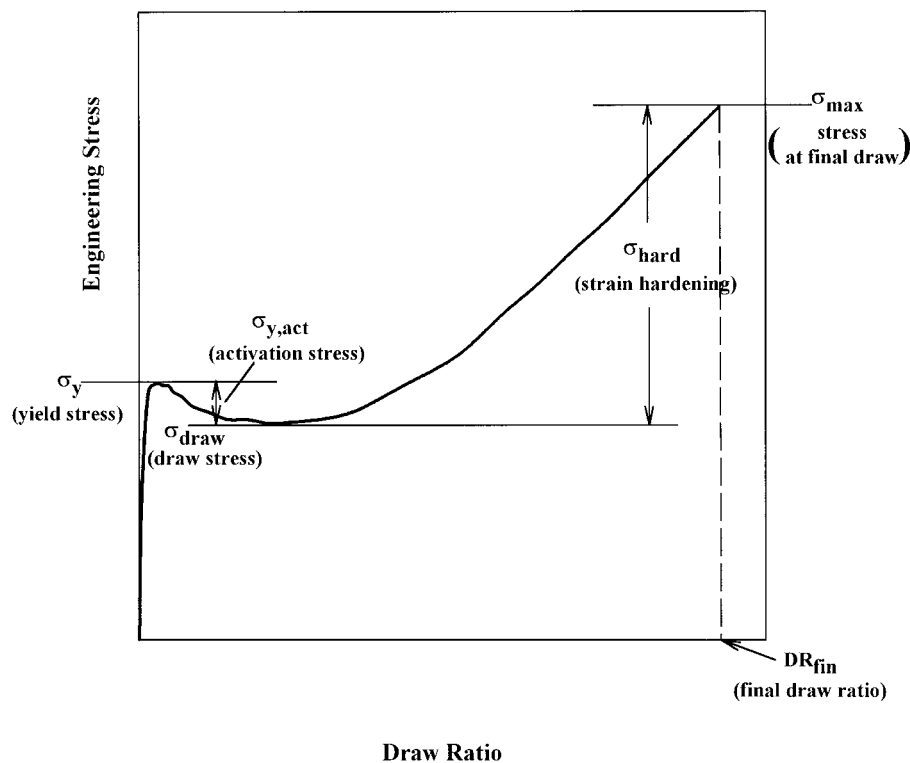Figure 5 shows the $f(T)$ derived from the DSC scans of each of the ZN-iPP and ZN-iPP/m-iPP

Figure 3 The definition of parameters derived from the elevated temperature draw stress curve. See text for discussion.
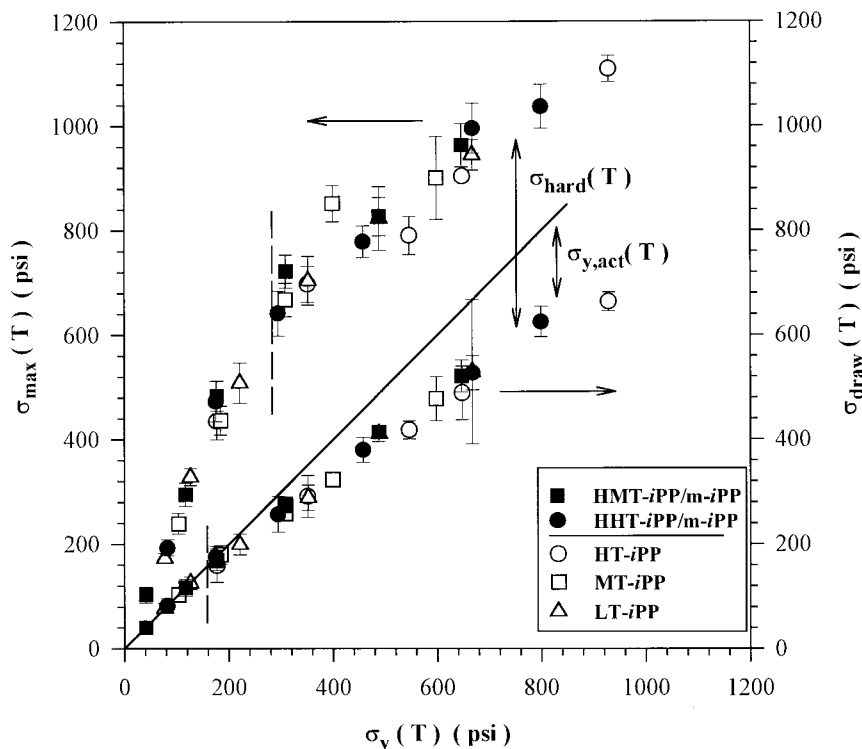
Figure 4 The interrelationships of parameters derived from the elevated tempera-ture draw stress curve for ZN-iPP (open symbols) and ZN-iPP/m-iPP blends (filled symbols). The draw curve parameters are defined in Figure 3.

blend samples. The addition of m-iPP to a ZN-iPP matrix increases the fractional melting relative to the ZN-iPP with a melting point comparable to the blend matrix component. This effect is due to the lower melting point of the m-iPP (Table I) and subsequent lowering of the blend melting point. This is seen clearly by the comparison of HT-iPP with the HHT-iPP/m-iPP blend and MT-iPP with the HMT-iPP/m-iPP blend. Figure 6 shows the empirical crystallinity index for each of the sam-ples. This index is described in the Experimental section. A comparison of Figure 2 and Figure 6 shows that the crystallinity index gives a reason-able qualitative ranking of the σ_y in the draw temperature region. Figure 6 shows that the de-pendence of the crystallinity index parameter on temperature has a different shape for the ZN-iPP/m-iPP blends relative to the ZN-iPP homopoly-mers. This shape change suggests a different bal-ance between the draw temperature crystallinity and the room temperature crystallinity. This con-clusion was supported by film density and crys-tallinity measurements.

Figure 7 shows the dependence of the film den-sity on the biaxial draw temperature for all of the
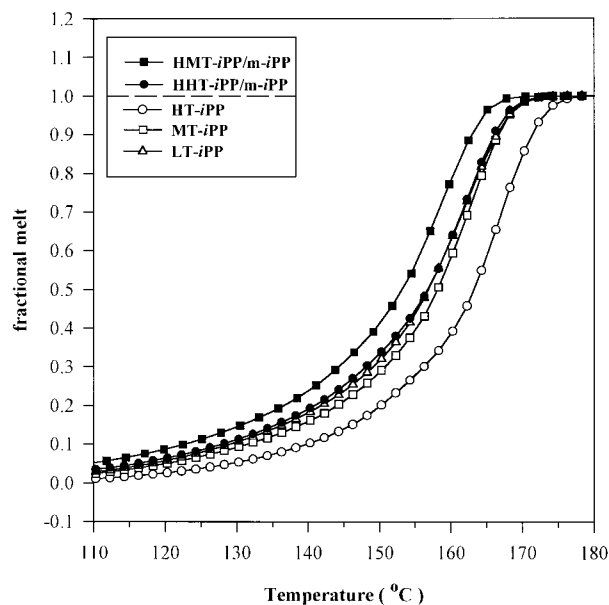

Figure 5 The fractional melting parameter derived from reheat DSC scans for ZN-iPP (open symbols) and ZN-iPP/m-iPP blends (filled symbols).
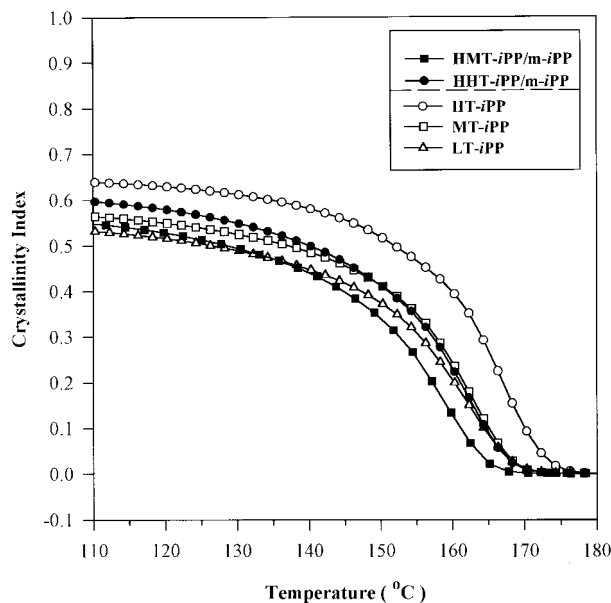
Figure 6 The crystallinity index parameter derived from reheat DSC scans for ZN-iPP (open symbols) and ZN-iPP/m-iPP blends (filled symbols).

samples. The ZN-iPP homopolymer and ZN-iPP/ m-iPP blend samples all show a strong increase in density with increasing draw temperature. The DSC heat of fusion data from selected films is shown in Figure 8. An increase of the heat of fusion with increasing draw temperature is ob-
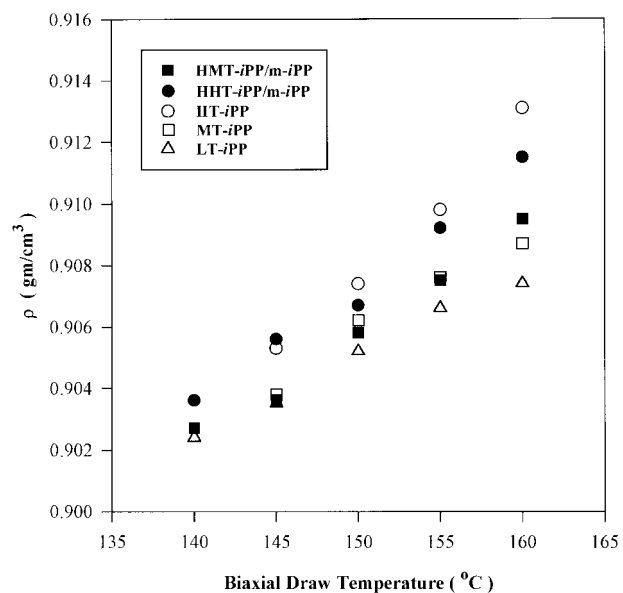

Figure 7 The room temperature BOPP film density, ρ, versus the initial draw temperature for ZN-iPP (open symbols) and ZN-iPP/m-iPP blends (filled symbols).
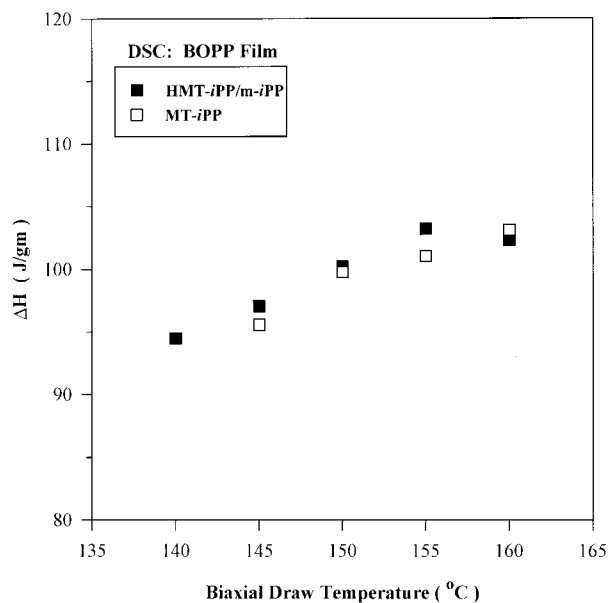

Figure 8 The DSC heat of fusion, ΔH, of selected BOPP films versus the initial draw temperature.

served. These data suggest that crystallinity in the final film increases with increasing draw temperature. A comparison of Figures 2 and 7 shows that the density of the films fabricated from the ZN-iPP/m-iPP blends is generally higher than the density of films from ZN-iPP resins with comparable elevated temperature yield stress $[\sigma_y(T)]$. This is illustrated by the comparison of HHT-iPP/ m-iPP with MT-iPP and the comparison of HMT-iPP/m-iPP with LT-iPP.

Figures 9 and 10 show the DSC melting traces of the HHT-iPP/m-iPP and HMT-iPP/m-iPP blends, respectively. Also shown are the predicted DSC traces derived from the weighted contribution of the DSC traces of the ZN-iPP and m-iPP components for each blend. Bimodal melting was predicted from the component behaviors. Experimentally, only a single melting endotherm was observed for both blends. A related effect was seen in the DSC crystallization cooling curves. A representative example is shown in Figure 11 for the HHT-iPP/m-iPP blend. In Figure 11 the crystallization cooling curve of the HHT-iPP/m-iPP blend is compared to the individual HHT-iPP matrix and m-iPP components. The individual blend components have widely separated crystallization temperatures. Based on this observation, two distinct crystallization exotherms were expected. However, this is not observed. The blend showed a sharp exotherm intermediate between the blend components and no signs of bimodality.
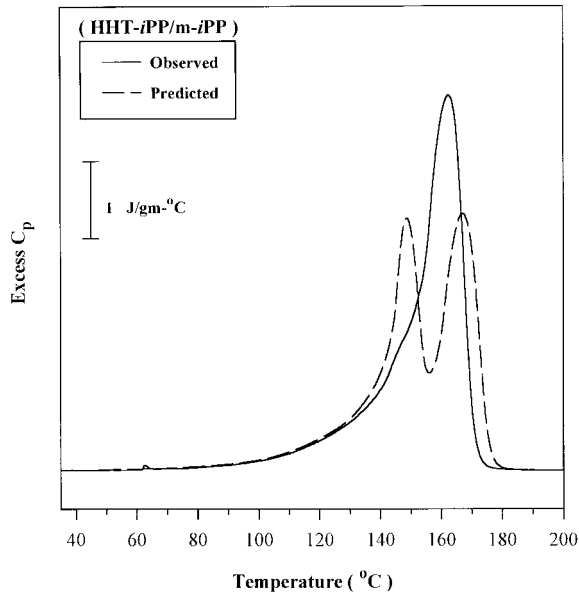
Figure 9 A DSC reheat scan of the (—) HHT-iPP/m-iPP blend versus the (- - -) predicted scan derived from the blend components.

Figure 11 A DSC cooling scan of the (- - -) HHT-iPP/m-iPP blend and the (—) individual HHT-iPP and m-iPP blend components.

Properties

Table II summarizes the tensile properties of the biaxially drawn film. Figure 2 shows the same $\sigma_y(T)$ for the HMT-iPP/m-iPP blend and LT-iPP resin. The same $\sigma_y(T)$ is also observed for the HHT-iPP/m-iPP blend and MT-iPP resin. Table II
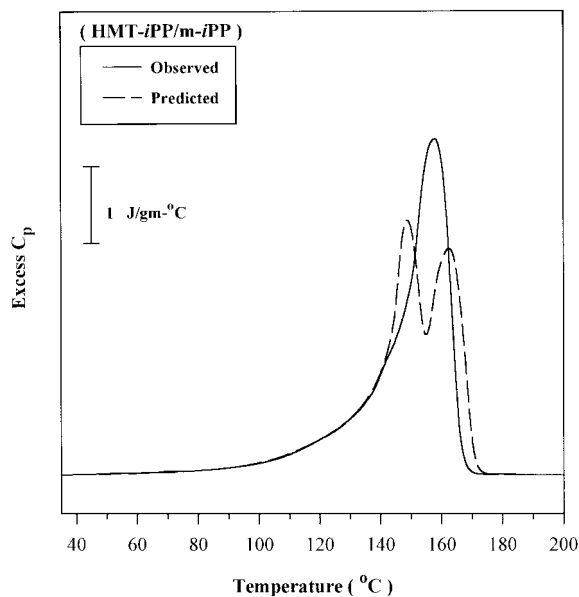

Figure 10 A DSC reheat scan of the (–) HMT-iPP/m-iPP blend versus the (- - -) predicted scan derived from the blend components.
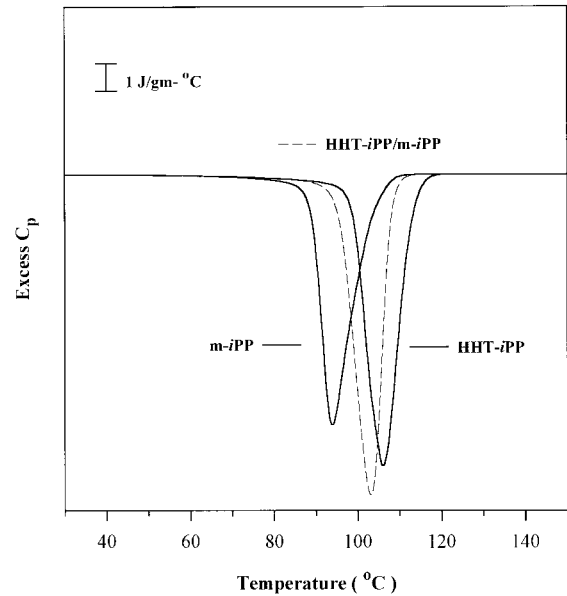
shows that the room temperature 1% secant modulus of the films formed from the ZN-iPP/m-iPP blends is higher than the modulus of films formed from ZN-iPP resins with similar elevated temperature $\sigma_y(T)$. In these films the ultimate elongation generally increases with increasing draw temperature. The films formed from the ZN-iPP/m-iPP blends drawn at 155°C show improved ultimate elongation relative to films formed from either ZN-iPP resins with comparable $\sigma_y(T)$ or ZN-iPP resins with melting points comparable to the blend matrix. Specifically, the elongation at break of the films drawn at 155°C from the HMT-iPP/m-iPP blend is higher than the LT-iPP amd MT-iPP films. A similar comparison applies to the HHT-iPP/m-iPP film with the MT-iPP and HT-iPP films drawn at 155°C.

Table III summarizes the oxygen barrier properties of films drawn at 145°C. The oxygen transmission is lower in films formed from the ZN-iPP/m-iPP blends relative to films formed from ZN-iPP resin with the same elevated temperature $\sigma_y(T)$. As discussed earlier, Figure 2 shows that the HMT-iPP/m-iPP blend has the same $\sigma_y(T)$ as the LT-iPP resin and the HHT-iPP/m-iPP blend has the same $\sigma_y(T)$ as the MT-iPP resin. The results in Table III show that for the same $\sigma_y(T)$, the oxygen transmission in the blends is lower. The combined results of Figure 2 and Tables II and III suggest that the ZN-iPP/m-iPP blends

Table II   Tensile Properties

	LT-iPP	HMT-iPP/m-iPP	MT-iPP	HHT-iPP/m-iPP	HT-iPP
Stretch temp. 145°C					
1% sec mod (MPa)	1905	2080	2130	2265	2580
Elongation at break (%)	101	87	82	103	98
Stretch temp. 150°C					
1% sec mod (MPa)	1990	2100	2120	2355	2720
Elongation at break (%)	94	99	87	95	93
Stretch temp. 155°C					
1% sec mod (MPa)	1920	1970	2100	2225	2730
Elongation at break (%)	130	148	101	116	94

sec mod, secant modulus.

exhibit a modified balance of elevated temperature draw (processing) characteristics and room temperature film properties relative to the ZN-iPP resins.

DISCUSSION

Figure 12 shows the σ_y data derived from Figure 2, which was evaluated at a range of stretch temperatures and correlated to parameters derived from a reheat DSC scan. The term $(1 - f)\Delta H_{\text{reheat}}$ is an empirical parameter that is intended to qualitatively represent the crystallinity at the draw temperature. The semilogarithmic representation parallels empirical correlations of yield stress to crystallinity in polyethylene[15] and flexural modulus in iPP.[20,32] The relationship of the empirical semilogarithmic model to limiting mixing rules is discussed elsewhere.[20] The relatively simple representation in Figure 12 does a surprisingly good job of collapsing into a common normalized form a wide variation of σ_y values (Fig. 2) that result from changes of draw temperature and resin microstructure. Figure 13 shows the same correlation on a linear scale. The solid line in Figure 13 is the same fit as shown in Figure 12.

The empirical nature of the parameter in Figure 12 chosen to represent the crystallinity at the draw temperature $[(1 - f)\Delta H_{\text{reheat}}]$ is strongly emphasized. The values of ΔH_{reheat} and $f(T)_{\text{reheat}}$ did not correspond to the crystallinity and melting characteristics in the as-cast sheet because of the DSC thermal cycle. Although not shown here, a very similar result was obtained when the ΔH and $f(T)$ were based on the first heat of the as-cast sheet, although the results differed quantitatively in a minor way. The reheat data were used to emphasize the predictive value of the approach when extending this formalism to new resins. More importantly, there was no direct correspondence between the DSC fractional crystallinity and that observed during film stretching because of a variety of experimental factors. Morphology development in the BOPP film was more complicated than Figures 12 and 13 infer. Important additional determinants of properties, both during drawing and in the final film, included the annealing processes and the molecular orientation–relaxation processes. The molecular weight variables were neglected by the fractional crystallinity model depicted in Figures 12 and 13. The temperature dependent yield effects (at fixed crystallinity)[27,29,51] were also neglected in the fractional crystallinity model. This effect causes the yield stress to decrease with increasing temperature, even without partial melting, although the temperature dependence observed in this

Table III   Oxygen Transmission

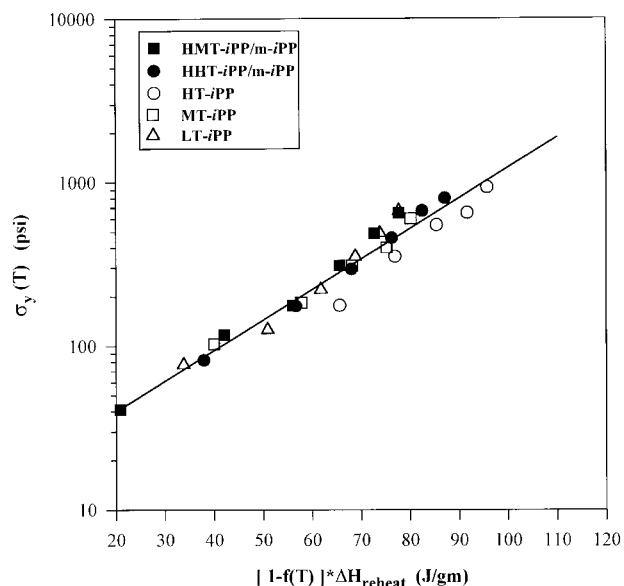|	LT-iPP	HMT-iPP/m-iPP	MT-iPP	HHT-iPP/m-iPP	HT-iPP
Stretch temp. 145°C					
Oxygen transmission (cm³/m² day)	1991	1678	1734	1404	1410

Figure 12 The semilogarithmic correlation of the biaxial engineering yield stress $\sigma_y(T)$ versus an empirical fractional crystallinity parameter $(1 - f)\Delta H_{\text{reheat}}$ derived from reheat DSC scans for ZN-iPP (open symbols) and ZN-iPP/m-iPP blends (filled symbols).

work was much stronger than predicted from the temperature effects alone.[27] Despite all of these complicating factors, the correlation in Figures 12 and 13 does a reasonable job of collapsing a wide range of yield behavior (Fig. 2) into a single unified representation. This simplified fractional crystallinity model (Figs. 12, 13) suggested two parameters that had a critical influence on the $\sigma_y(T)$ for iPP. These were the $f(T)$ and the resin crystallizability represented by ΔH_{reheat}. The draw temperature and aspects of the resin tacticity (melting point) both influenced the $f(T)$. The influence of tacticity and the addition of m-iPP to a ZN-iPP matrix in the blends on the $f(T)$ is shown in Figure 5. The ΔH_{reheat} is also influenced by aspects of the resin tacticity.[30–33] Additionally, the correlation of $\sigma_y(T)$ with the fractional crystallinity parameter was nonlinear (Fig. 13). This is a feature of the semilogarithmic mixing rule.[20] This observation suggested that resins with low $\sigma_y(T)$ should be less sensitive to process temperature variations through the influence of the $f(T)$, because they lie on the flatter portion of this correlation.

Table I shows that the m-iPP used in this study had a much lower melting point than the ZN-iPP resins. The measureable concentration of regioerrors contributed to this low melting point.[33–35,40,47] The low melting point in the context of Figures 12

and 13 suggested that addition of the m-iPP to a ZN-iPP matrix should lower the $\sigma_y(T)$. This is what is observed in Figure 2. The HT-iPP resin and HHT-iPP component in the HHT-iPP/m-iPP blend had comparable melting points (Table I), but the blend exhibited much lower σ_y. Similarly, the MT-iPP and HMT-iPP component in the HMT-iPP/m-iPP blend had comparable melting points, but the blend exhibited lower σ_y. The lowering of the $\sigma_y(T)$ by adding m-iPP to a ZN-iPP matrix was similar to the effect of decreasing the stereospecificity in conventional ZN-iPP BOPP resins (Fig. 2). However, despite the low melting point of the m-iPP, the crystallinity was not markedly different from the ZN-iPP homopolymer resins with similar stereospecificity.[33] Consequently, the addition of m-iPP as a means of reducing $\sigma_y(T)$ only modestly reduced the film density. This is shown in Figure 7.

The film density data in Figure 7 indicate that the homopolymer and blend samples all showed a strong increase in density with increasing stretch temperature. Two primary factors can contribute to this behavior. The incidence of microvoiding, which can be prevalent during iPP deformation at low temperature,[27,52] may decrease with increasing temperature. This could contribute to the large increase of density with increasing draw temperature. Alternatively, the density change
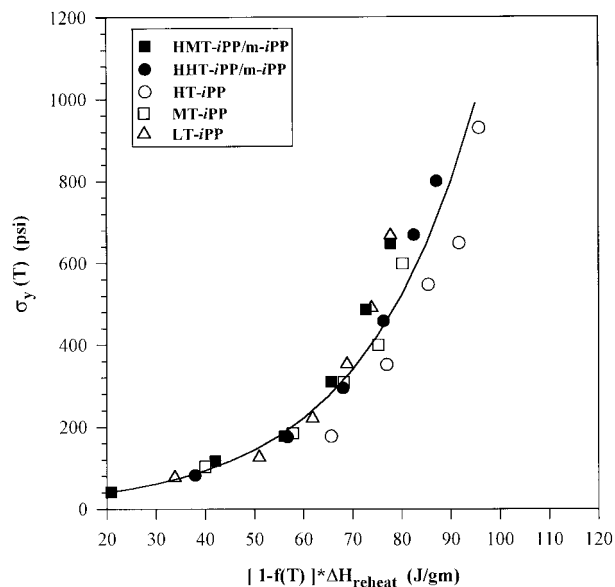

Figure 13 The linear correlation of the biaxial engineering yield stress $\sigma_y(T)$ versus an empirical fractional crystallinity parameter $(1 - f)\Delta H_{\text{reheat}}$ derived from reheat DSC scans for ZN-iPP (open symbols) and ZN-iPP/m-iPP blends (filled symbols).

may be due to an increase in crystallinty and/or crystallite perfection. Figure 8 shows the heat of fusion of selected as-drawn films as a function of draw temperature. The heat of fusion measurement should not be influenced by effects related to microvoiding. The increase of the heat of fusion with increasing draw temperature in Figure 8 indicates that the increase of density in Figure 7 was predominantly attributable to an increase in crystallinity in the final film. This increase can be due to both annealing and deformation of the solidlike component during stretching and higher crystallinity from fractions that are liquidlike during drawing but crystallize during cooling under relatively slow cooling conditions relative to the original sheet casting conditions. These effects are not separated in the current study. However, the latter mechanism must have played an important contributing role, because the amount of material that was solidlike at the draw temperature decreased in the melting range as evidenced from the elevated temperature draw behavior (Fig. 2).

Examination of details of the melting behavior and density data illustrated the altered crystallinty and melting balance in the ZN-iPP/m-iPP blends. As already discussed, this observation can be inferred from the behavior of the m-iPP homopolymer.[33] A comparison of Figures 5 and 6 further emphasizes the rationale of taking into account the fractional melting and resin crystallizability in the correlative scheme of Figures 12 and 13. A comparison of Figures 2 and 5 shows that if only fractional melting characteristics were considered, a very different ranking of $\sigma_y(T)$ between the various samples would be predicted relative to the observed behavior. However, Figures 2 and 6 give a reasonable correlation of the observed behavior in terms of the empirical fractional crystallinity parameter. Because the fractional melting parameter is a rough analog to the stereoblock content,[32] these comparisons emphasize the very different stereoblock–draw relationships in the ZN-iPP/m-iPP blends versus that of the ZN-iPP homopolymers. This contrasting property balance was also observed in the room temperature crystallinity–draw balance. A comparison of LT-iPP with HMT-iPP/m-iPP and MT-iPP with HHT-iPP/m-iPP in Figures 2 and 7 shows that the ZN-iPP/m-iPP blends have higher room temperature film density, particularly at high stretch temperatures, relative to the ZN-iPP with the same $\sigma_y(T)$. In the ZN-iPP resins the $\sigma_y(T)$ data had a direct correspondence to the final film

density. The ZN-iPP/m-iPP blends partially circumvent this processing–property balance.

A comparison of Figure 2 and Table II shows a similar modification of the processing–property balance in the ZN-iPP/m-iPP blends. A comparison of LT-iPP with HMT-iPP/m-iPP and MT-iPP with HHT-iPP/m-iPP shows that for the same $\sigma_y(T)$, the ZN-iPP/m-iPP blends showed improved room temperature modulus relative to ZN-iPP. Interestingly, in the context of the strong increase in density with increasing draw temperature in Figure 7, the modulus of the films showed a comparatively weak dependence on the draw temperature (Table II). The modulus of iPP is expected to increase strongly with increased density.[14,20,21,32,33] Literature reports suggest that the orientation decreases with increasing draw temperature.[53] This conclusion is consistent with the expectation that the increasing liquidlike fractions formed with increasing draw temperature are not expected to sustain high orientation levels following crystallization on cooling. This hypothesis is also supported by the increase of elongation at break at higher draw temperatures for most samples (Table II). The increase in elongation at break at higher draw temperature is larger in the blends and homopolymer with lower $\sigma_y(T)$, supporting the notion that increased fractional melting leads to less orientation in the final film. Consequently, two competing effects appeared to operate with increasing draw temperature in the final film. The crystallinity increased, but the orientation decreased. These competing effects, directly observed in literature reports,[53] appeared to limit the dependence of the modulus on the draw temperature. An additional consideration was the improved modulus–elongation balance observed in the ZN-iPP/m-iPP blends at elevated draw temperatures. As discussed, the stronger dependence of the elongation at break on the draw temperature in the homopolymers and blends with low $\sigma_y(T)$ can be rationalized by a loss of orientation and an increase of liquidlike fractions at the draw temperature. As discussed above in the context of Figures 5 and 6, the ZN-iPP/m-iPP blends were expected to exhibit higher fractional melting relative to both the ZN-iPP with a melting point comparable to the blend matrix and the ZN-iPP with an equivalent $\sigma_y(T)$. It was then consistent to observe higher elongation at break values in the ZN-iPP/m-iPP blends relative to the comparative homopolymer pairs at higher draw temperatures. The elongation at break (Table II) of the films drawn at 155°C from the HMT-iPP/m-iPP blend

was higher than the LT-iPP amd MT-iPP films. A similar comparison applied to the HHT-iPP/m-iPP film with the MT-iPP and HT-iPP films drawn at 155°C. Accompanying the apparent orientation differences, however, was a higher crystallizability of both the liquidlike and solidlike fractions of the ZN-iPP/m-iPP blend relative to the homopolymer with equivalent $\sigma_y(T)$. Consequently, two competing effects existed in the ZN-iPP/m-iPP blends, which gave rise to a unique property balance. Higher elongations (at high draw temperature) relative to the ZN-iPP with a melting point comparable to the blend matrix and the ZN-iPP with an equivalent $\sigma_y(T)$ were observed, but the modulus values were intermediate between these two limiting cases. A similar property synergy was seen in the oxygen transmission results. Comparing LT-iPP with HMT-iPP/m-iPP and MT-iPP with HHT-iPP/m-iPP in Figure 2 and Table III shows that for the same $\sigma_y(T)$ the ZN-iPP/m-iPP blends exhibited reduced oxygen permeability.

An additional morphological consideration in any multicomponent mixture is the detailed nature of the segregation of blend components. Although m-iPP and ZN-iPP were expected to be miscible in the melt, a physical separation of the blend components might be expected to occur on crystallization because of the very different crystallization temperatures (Fig. 11) and thermodynamic undercooling for crystallization suggested by the different melting points. Recent work showed the much slower crystallization rate of low melting point m-iPP relative to high melting point ZN-iPP.[54] Consequently, it might be expected that m-iPP segregates within the morphology because of the fact that it crystallizes later on cooling. However, this type of segregation did not appear to occur to the extent expected for ZN-iPP/m-iPP blends during crystallization at high undercooling. Figure 11 shows that for the specific case of the HHT-iPP/m-iPP blend, the individual blend components showed widely separated crystallization temperatures. Based on this, two distinct crystallization exotherms were expected in the blend. This is not observed in Figure 11, however. The blend shows a sharp crystallization exotherm intermediate between the blend components and no signs of bimodality. This result suggested cocrystallization of the blend components. This conclusion was further supported by the DSC melting results in Figures 9 and 10. Figures 9 and 10 show the DSC melting traces of the HHT-iPP/m-iPP and HMT-iPP/m-iPP blends, re-

spectively. Superposed on both figures is the predicted melting behavior, which was based on the weighted contributions of the blend components. In both cases the observed DSC result did not match the predicted trace. The blends showed a single DSC melting peak intermediate between the two peaks predicted by the component behaviors. This departure of the observed melting curves from the predicted curves was consistent with cocrystallization of the blend components.[55–57] A morphology determined by cocrystallization of the blend components can have implications on other aspects of the deformation behavior, as discussed shortly.

Earlier discussions suggested that the $\sigma_y(T)$ could be adequately described by a simplified fractional crystallinity model. At the same value of the fractional crystallinity parameter, there was little difference in the σ_y between the ZN-iPP homopolymers and ZN-iPP/m-iPP blends. Figure 4 shows the relationship between σ_{max} and σ_{draw} with the σ_y for all of the samples and draw temperatures investigated. These parameters are defined in Figure 3. From Figure 4 there appeared to be very similar relationships for the ZN-iPP and ZN-iPP/m-iPP blends. The correlations in Figure 4 to $\sigma_y(T)$ suggest an expanded utility of the fractional crystallinity concept to other aspects of the deformation behavior. Furthermore, the details of the relationships in Figure 4 illustrate additional aspects of the morphology during stretching. The σ_{draw} coincides with σ_y at low values of σ_y, because there was no stress maxima at low crystallinity levels. Above a certain value of σ_y, the σ_{draw} began to deviate from the $\sigma_{draw} = \sigma_y$ line. This deviation became larger as the σ_y (and the crystallinity) increased. Above a critical σ_y (crystallinity) (marked by dashed line on the σ_{draw} curve), the $\sigma_{y,act}$ increased with increased σ_y. This change of the σ_y was accomplished by increasing the resin crystallinity or decreasing the draw temperature for a given resin. The behavior of σ_{max} can be similarly differentiated, although the differentiation occurred at a different σ_y (crystallinity) level. At low values of σ_y, the σ_{max} rapidly increased up to a dividing line in σ_y (marked by dashed line on the σ_{max} curve). Beyond this value of σ_y the σ_{max} increased more gradually, roughly maintaining a constant relationship with the σ_{draw}.

The transitional mechanical behavior for BOPP film drawing of ZN-iPP and ZN-iPP/m-iPP blends is more clearly illustrated in Figure 14 by plotting the difference quantities σ_{hard} and $\sigma_{y,act}$
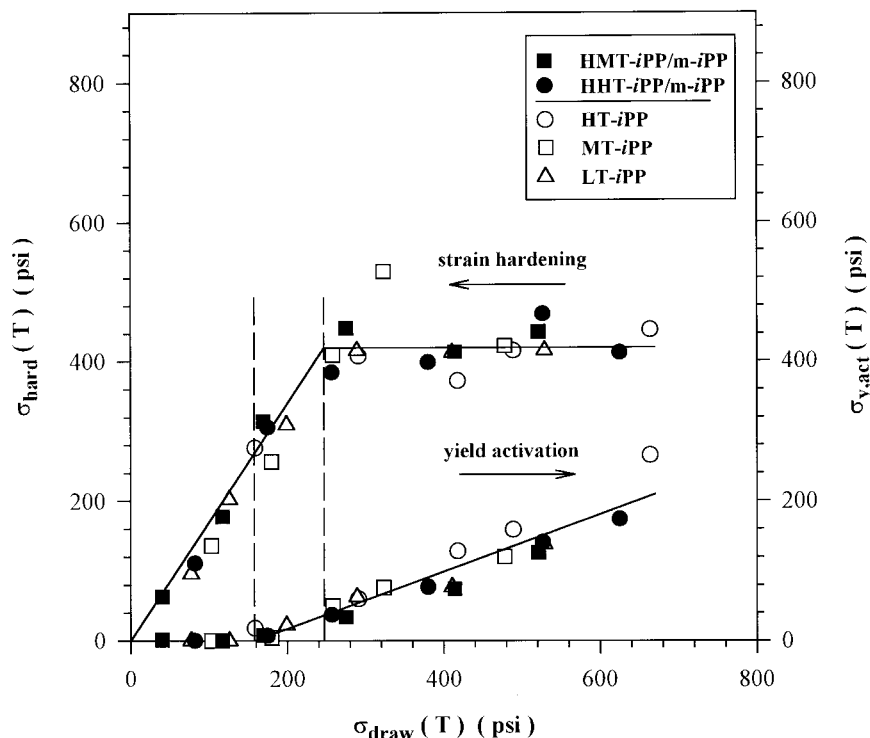
Figure 14   Parameters quantifying the strain hardening $\sigma_{\mathrm{hard}}(T)$ and yield activation $\sigma_{\mathrm{y,act}}(T)$ versus the draw stress $\sigma_{\mathrm{draw}}(T)$ for ZN-iPP (open symbols) and ZN-iPP/m-iPP blends (filled symbols). The draw curve parameters are defined in Figure 3.

versus σ_{draw}. As discussed in the context of Figure 4, similar relations can be made in terms of σ_y. A clear transitional behavior was observed that was related to the yield activation and strain hardening. Although the σ_{draw} increased with the σ_y (crystallinity) for all σ_y levels (Fig. 4), above a critical transitional value the σ_y increased more strongly. Thus, the crystallinity increased the stress required for region III transformation and also more strongly increased the stress required to initiate yielding (yield activation). Perhaps more intriguing was the strain hardening behavior. At low σ_{draw} (crystallinity) the strain hardening strongly increased up to a transitional value. Beyond this transitional value the strain hardening appeared to be independent of the σ_{draw} (crystallinity). The σ_{max} increased in proportion to the σ_{draw}. In the context of uniaxial deformation models, this suggested that above a certain crystallinity level the stress associated with orienting the fibrillar morphology (region IV strain hardening) depended only on the draw ratio, not the crystallinity level. However, there was a baseline contribution of crystallinity to the σ_{draw}, which increased continuously with increasing crystallinity.

These experimental observations suggested a crystallinity independent orientation stress, and it paralleled earlier attempts to "decouple" orientation and crystallinity contributions to mechanical properties of oriented moldings of iPP by treating the contributions independently.[20] For extensions up to the $\mathrm{DR_{fin}}$, the transitional strain hardening behavior in Figure 14 was consistent with certain aspects of uniaxial deformation models at high extensions.[3,4] During region IV deformation (Fig. 1), drawing is associated with a fibrillar morphology, presumably fully transformed from the initial lamellar–spherulitic morphology. Deformation in this region is strongly related to the tie molecule content according to most fibrillar deformation models.[3,4,58] In addition to tie molecule considerations, Figure 4 suggests a clear baseline contribution of crystallinity to the deformation stress in this region. That is, increased crystallinity increased the drawing stress, which provided a baseline contribution to the subsequent deformation stress. A reasonable assumption for the uniaxial deformation of iPP at room temperature was to neglect strain-induced crystallization effects.[59] If this effect is neglected during elevated temperature biaxial stretching,

then the σ_{hard} can be viewed as the force required to deform the fibrillar structure, irrespective of the crystallinity level. With this assumption the σ_{hard} may have a qualitative interpretation in terms of uniaxial tie molecule deformation models.[3,4]

Partial melting during the highest temperature drawing experiments caused large decreases in the σ_y (Fig. 2) and the empirical crystallinity parameter (Fig. 6). Because the deformation-induced tie molecule content must be closely related to the crystallinity level,[60] the σ_{hard} decreased in this regime. The appearance of a plateau region in Figure 14 at high σ_{draw} (crystallinity) suggests that the deformation-induced tie molecule content did not increase indefinitely with increasing crystallinity. The tie molecule content was fully developed at a critical crystallinity level, irrespective of the resin–blend type or draw temperature. That is, the drawing-induced tie molecule content, which increased with increasing draw ratio,[4] was fully determined by the final draw ratio provided the crystallinity (determined by the draw temperature and melting characteristics) was greater than a critical value. This implied that within this hardening plateau region the orientation of the solidlike component during drawing was insensitive to the crystallinity level, although the relative proportions of the solidlike and liquidlike fractions (differing in orientation) were markedly changed.

At lower crystallinity levels (below transitional value), the notion of increasing tie molecule content with increasing crystallinity was in agreement with room temperature deformation results of linear low-density polyethylene.[60] In linear low-density polyethylene the semitheoretical arguments suggested that the tie molecule concentration and corresponding strain hardening should increase with crystallinity up to a maximum followed by a decrease.[60] This was qualitatively consistent with the current observations for elevated temperature biaxial drawing of iPP, although a decrease at higher σ_{draw} (crystallinity) was not observed (for the range of crystallinities and draw temperatures investigated). Similar arguments were applied to suggest an increase of tie molecule concentration with increasing molecular weight and to explain the increased strain hardening observed in polyethylene with increasing molecular weight.[19,60] This latter issue was relevant to the ZN-iPP/m-iPP blends. Because these blends had a high molecular weight ZN-iPP component, it might have been expected that the

solidlike component during drawing would exhibit increased strain hardening (at fixed crystallinity) relative to the homopolymer resins.[19,60,61] This was not observed, however. Figures 4 and 14 show that nearly all aspects of the deformation behavior of the blends and homopolymer resins very nearly superpose. This mechanical behavior indirectly supported the notion of cocrystallization of the blend components previously discussed in the context of Figures 9–11. In this context neither the melting nor drawing characteristics discriminated between the individual molecular weights of the blend components. Only the average molecular weight characteristics of the blend influenced the behaviors (which in this study were closely matched to the homopolymer resins). Consequently, this provided an explanation why the high molecular weight component in the blend was not fully realized in the mechanical behavior.

In this study an overly simplistic, although useful, picture of the morphology of BOPP film drawn within the partial melting zone was that of a morphology crudely partitioned between oriented and unoriented components that were correlated to the solidlike and liquidlike components at the draw temperature. As discussed, this simplistic viewpoint was used to describe a variety of effects relating to the influence of draw temperature and resin–blend characteristics on properties such as the draw behavior, film stiffness, barrier, and elongation. A further detailed understanding of the formation and morphology of these partitioned components is needed to fully explain all aspects of the property balance in a quantitative way. Particularly important in this regard is an understanding of the crystallinities of the solidlike and liquidlike components and orientation retention after cooling from the draw temperature.

CONCLUSIONS

The structure, processing, morphology, and property relations of BOPP films from ZN-iPP and blends of ZN-iPP with m-iPP were evaluated. The ZN-iPP/m-iPP blends were prepared from a low melting, low molecular weight m-iPP and a high melting, high molecular weight ZN-iPP. The structure–property relations of these blends were compared to a ZN-iPP homopolymer with a range of isotacticities (melting points). The morphology

of the blends showed cocrystallization of the ZN-iPP and m-iPP, which influenced aspects of the deformation behavior at elevated temperature. At fixed draw temperature the addition of m-iPP to the ZN-iPP matrix was shown to lower the $\sigma_y(T)$ relative to a ZN-iPP homopolymer with a melting point similar to the blend matrix. In addition to lowering the biaxial yield stress, the addition of the m-iPP component gave rise to improvements of the film modulus relative to ZN-iPP resins with the same $\sigma_y(T)$. Improvements in elongation at break and room temperature oxygen transmission were also observed relative to ZN-iPP with the same $\sigma_y(T)$. A simplified fractional crystallinity model was developed, which viewed the yield stress (at equivalent molecular weight) as being controlled by the crystallinity at the draw temperature. According to this viewpoint, the yield stress during high temperature drawing was governed by both the overall resin–blend crystallizability and the melting distribution. The model successfully collapsed all of the $\sigma_y(T)$ data into a single normalized representation over a range of draw temperatures, ZN-iPP resin tacticities, and ZN-iPP/m-iPP blend compositions. The model was extended to other aspects of the deformation, including analogies with uniaxial deformation models relating to the lamellar–fibrillar transformation and fibrillar deformation regimes. Interrelationships were developed that defined yield activation and strain hardening behavior into regimes differentiated by characteristic crystallinity levels. A simplistic view of the morphology in the final film was that of a morphology crudely partitioned between oriented and unoriented components that were correlated to the solidlike and liquidlike components at the draw temperature. This viewpoint described a variety of effects relating to the effects of draw temperature and resin and blend characteristics on the properties such as the draw behavior, film stiffness, barrier, and elongation. In general, the results also showed that the ZN-iPP/m-iPP blends shifted the processability–property balance in the BOPP film relative to the iPP homopolymer from Ziegler–Natta catalysts.

REFERENCES

1. Samuels, R. J. J Polym Sci (A2) 1968, 6, 1101.
2. Samuels, R. J. Structured Polymer Properties: The Identification, Interpretation, and Application of Crystalline Polymer Structure; Wiley: New York, 1974.
3. Peterlin, A. Polym Eng Sci 1977, 17, 183.
4. Peterlin, A. Colloid Polym Sci 1987, 265, 357.
5. Lin, L.; Argon, A. S. J Mater Sci 1994, 29, 294.
6. G'Sell, C.; Dahoun, A.; Favier, V.; Hiver, J. M.; Philippe, M. J.; Canova, G. R. Polym Eng Sci 1997, 37, 702.
7. Butler, M. F.; Donald, A. M.; Ryan, A. J. Polymer 1997, 38, 5521.
8. Butler, M. F.; Donald, A. M.; Ryan, A. J. Polymer 1998, 39, 39.
9. Kerner, E. H. Proc Phys Soc 1956, 69(B), 808.
10. Takayangi, M.; Imada, K.; Kajiyama, T. J Polym Sci 1966, 15, 263.
11. Gray, R. W.; McCrum, N. G. J Polym Sci 1969, 7, 1329.
12. Halpin, J. C.; Kardos, J. D. J Appl Phys 1972, 43, 2236.
13. Boyd, R. H. Polym Eng Sci 1979, 19, 1010.
14. Seferis, J. C.; Samuels, R. J. Polym Eng Sci 1979, 19, 975.
15. Christ, B.; Fischer, C. J.; Howard, D. R. Macromolecules 1989, 22, 1709.
16. Peacock, A. J.; Mandelkern, L. J Polym Sci Polym Phys 1990, 28, 1917.
17. Janzen, J. Polym Eng Sci 1992, 32, 1242.
18. Sehanobish, K.; Patel, R. M.; Croft, B. A.; Chum, S. P.; Kao, C. I. J Appl Polym Sci 1994, 51, 887.
19. Kennedy, M. A.; Peacock, A. J.; Mandelkern, L. Macromolecules 1994, 27, 5297.
20. Phillips, R. A.; Hebert, G.; News, J.; Wolkowicz, M. Polym Eng Sci 1994, 34, 1731.
21. Van der Wal, A.; Mulder, J. J.; Gaymans, R. J. Polymer 1998, 39, 5477.
22. Mandelkern, L. Polym J 1985, 17, 337.
23. Flory, P. J.; Yoon, D. Y. Nature 1978, 272, 226.
24. Darras, O.; Seguela, R. J Polym Sci Polym Phys 1993, 31, 759.
25. Annis, B. K.; Strizak, J.; Wignall, G. D.; Alamo, R. G.; Mandelkern, L. Polymer 1996, 37, 137.
26. Argon, A. S. Phil Mag 1973, 28, 839.
27. Liu, Y.; Truss, R. W. J Polym Sci Polym Phys 1994, 32, 2037.
28. Brooks, N. W. J.; Duckett, R. A.; Ward, I. M. J Rheol 1995, 39, 425.
29. Seguela, R.; Staniek, E.; Escaig, B.; Fillon, B. J Appl Polym Sci 1999, 71, 1873.
30. Burfield, D. R.; Loi, P. S. T.; Doi, Y.; Majzik, J. J Appl Polym Sci 1990, 41, 1095.
31. Paukkeri, R.; Lehtinen A. Polymer 1993, 34, 4075.
32. Phillips, R. A.; Wolkowicz, M. D. In Polypropylene Handbook; Moore, E. P., Ed.; Hanser: Munich, 1996; p 113.

33. Haylock, J. C.; Phillips, R. A.; Wolkowicz, M. D. In Metallocene Based Polyolefins: Preparation, Properties and Technology; Scheirs, J., Kamisky, W., Eds.; Wiley: Chichester, UK, 2000; Vol. 2, p 333.

34. Brintzinger, H. H.; Fischer, D.; Mulhaupt, R.; Rieger, B.; Waymouth, R. M. Angew Chem Int Ed Engl 1995, 34, 1143.

35. Tsutsui, T.; Ishimaru, N.; Mizumo, A.; Toyota, A.; Kashiwa, N. Polymer 1989, 30, 1350.

36. Tsutsui, T.; Kashiwa, N.; Mizuno, A. Makromol Chem Rapid Commun 1990, 11, 565.

37. Cheng, H. N.; Ewen, J. A. Makromol Chem 1989, 190, 1931.

38. Soga, K.; Shiono, T.; Takemura, S.; Kaminsky, W. Makromol Chem Rapid Commun 1987, 8, 305.

39. Grassi, A.; Zambelli, A.; Resconi, L.; Albizzati, E.; Mazzocchi, R. Macromolecules 1988, 21, 617.

40. Toyota, A.; Tsutsui, T.; Kashiwa, N. J Mol Catal 1989, 56, 237.

41. Chien, J. C. W.; Sugimoto, R. J Polym Sci Polym Chem 1991, 29, 459.

42. Resconi, L.; Fait, A.; Piemontesi, F.; Colonnesi, M.; Rychlicki, H.; Zeigler, R. Macromolecules 1995, 28, 6667.

43. Roll, W.; Brintzinger, H.-H.; Rieger, B.; Zolk, R. Angew Chem Int Ed Engl 1990, 29, 279.

44. Rieger, B.; Mu, X.; Mallin, D. T.; Rausch, M. D.; Chien, J. C. W. Macromolecules 1990, 23, 3559.

45. Fischer, D.; Mulhaupt, R. Macromol Chem Phys 1994, 195, 1433.

46. Stehling, U.; Diebold, J.; Kirsten, R.; Roll, W.; Brintzinger, H. H.; Jungling, S.; Mulhaupt, R.; Langhauser, F. Organometallics 1994, 13, 964.

47. Hungenberg, K. D.; Kerth, J.; Langhauser, F.; Marczinke, B.; Schlund, R. In Ziegler Catalysts; Mulhaupt, R., Brintzing, H. H., Eds.; Springer: Berlin, 1995.

48. Langhauser, F.; Kerth, J.; Kersting, M.; Kolle, P.; Lilge, D.; Muller, P. Angew Makromol Chem 1994, 223, 155.

49. Mehta, A. K.; Chen, M. C.; McAlpin, J. J. Presented at the Society of Plastic Engineers RETEC 97 conference, Houston, TX, 1997.

50. Doi, Y. Makromol Chem Rapid Commun 1982, 3, 635.

51. Seguela, R.; Darras, O. J Mater Sci 1994, 29, 5342.

52. Liu, Y.; Kennard, C. H. L.; Truss, R. W.; Calos, N. J. Polymer 1997, 38, 2797.

53. Taraiya, A. K.; Orchard, G. A. J.; Ward, I. M. J Appl Polym Sci 1990, 41, 1659.

54. Phillips, R. A. ACS Polym Mater Sci Eng Polym Prepr 1999, 81, 376.

55. Hu, S.-R.; Kyu, T.; Stein, R. S. J Polym Sci Polym Phys 1987, 25, 71.

56. Tashiro, K.; Stein, R. S.; Hsu, S. L. Macromolecules 1992, 25, 1801.

57. Tashiro, K.; Izuchi, M.; Kobayashi, M.; Stein, R. S. Macromolecules 1994, 27, 1221.

58. Takayanagi, M.; Nitta, H.-H. Macromol Theory Simul 1997, 6, 181.

59. Samuels, R. J. J Polym Sci (A) 1965, 3, 1741.

60. Hosada, S.; Uemura, A. Polym J 1992, 24, 939.

61. Baranov, A. O.; Prut, E. V. J Appl Polym Sci 1992, 44, 1557.